Chemical Science

ROYAL SOCIETY OF CHEMISTRY

EDGE ARTICLE

View Article Online
View Journal | View Issue

Cite this: *Chem. Sci.*, 2025, **16**, 18332

All publication charges for this article have been paid for by the Royal Society of Chemistry

Received 23rd July 2025
Accepted 1st September 2025

DOI: 10.1039/d5sc05501f

rsc.li/chemical-science

Peripherally fused spiro structures enable the development of narrowband TADF emitters for highly efficient blue OLEDs

Deli Li, †[a] Denghui Liu,†[c] Mengke Li,†[c] Qingchao Liu,[a] Wei Liu,[a] Wei Li, *[b] Shi-Jian Su *[c] and Xuchuan Jiang *[a]

To address the spectral broadening and red shift inherent in multi-resonance thermally activated delayed fluorescence (MR-TADF) emitters, which are caused by aggregation due to their planar structures, we propose a strategic fusion of spiro groups at specific peripheral positions within the classic narrowband emitter DABNA core. Leveraging positional isomerism, this innovative approach enables the development of two blue TADF emitters: SFX-2BN (O-π-B) and SFX-3BN (O-π-N). The relative positioning of the electron-withdrawing boron (B) and electron-donating nitrogen (N) atoms around the oxygen enables precise emission tuning from sky-blue to pure blue. The rigid spiro structure acts as an intramolecular lock, effectively suppressing detrimental vibrations and π–π stacking, thereby yielding exceptionally narrowband emission (FWHM = 20–22 nm) for both isomers. They exhibit high photoluminescence quantum yields (PLQYs >90%) in thin films. Corresponding OLEDs achieve maximum external quantum efficiencies (EQEs) of 24.8% and 33.4%, respectively. Furthermore, by employing a TADF assistant host, the OLED based on SFX-2BN is improved to 27.5%, while maintaining excellent color purity, with CIE coordinates (0.14, 0.06), which closely approach the BT.2020 blue standard. These results provide key mechanistic insights into the narrowing of emission bands through spiro-group fusion at specific positions within the MR core.

Introduction

Thermally activated delayed fluorescence (TADF) emitters based on polycyclic aromatic hydrocarbon (PAH) structures combined with the multi-resonance (MR) effect offer a promising approach for narrowband emission.[1–3] Typically, MR-TADF emitters featuring rigid PAH frameworks combined with electron-donating and electron-withdrawing atoms enable a complementary resonance effect and promote atomic-level highest occupied molecular orbital (HOMO)–lowest unoccupied molecular orbital (LUMO) separation. Consequently, this approach allows for small ΔE_{ST} and efficient TADF performance. Significantly, the rigid molecular skeletons and reduced bonding/antibonding interactions in MR emitters effectively suppress molecular vibrational relaxation, resulting in narrowband emission with full width at half maximum (FWHM) values below 30 nm.[4–6] Since the pioneering work by Hatakeyama and colleagues in 2016,[1] various PAH skeletons with diverse elemental compositions, such as B/N- and C=O/N-based structures, have been developed for MR-TADF applications.[7–9] In addition, the planar and rigid PAH molecular skeleton of MR-TADF emitters enhances optical out-coupling efficiency, thereby improving device performance. However, this planar design also leads to intermolecular interactions among the emitters in the aggregated state, resulting in red-shifted emission and a broader spectrum.[10–12] To address the quenching issue caused by molecular aggregation in MR-TADF emitters, which is attributed to their planar structure, several strategies have been proposed.[13–15] Among these, modifying spiro structures is widely recognized as one of the most effective methods for achieving better results.

Spiral units offer significant advantages in the development of efficient TADF emitters[16–19] and host materials.[20] The substantial steric hindrance imparted by the spiral fragment leads to a marked increase in the intermolecular distance between adjacent molecules, thereby reducing intermolecular interactions and mitigating the aggregation-caused quenching (ACQ) effect.[17,21] One method for constructing MR-TADF emitters involves using spiral donor units, which have strong electron-donating capabilities and a six-membered ring structure,

[a]*Institute for Smart Materials & Engineering, University of Jinan, Jinan, 250022, P. R. China. E-mail: ism_jiangxc@ujn.edu.cn*

[b]*Zhejiang Provincial Engineering Research Center of Energy Optoelectronic Materials and Devices, Ningbo Institute of Materials Technology and Engineering, Chinese Academy of Sciences, Ningbo, 315201, P. R. China. E-mail: liwei1987@nimte.ac.cn*

[c]*Guangdong Basic Research Center of Excellence for Energy and Information Polymer Materials, Institute of Polymer Optoelectronic Materials and Devices, State Key Laboratory of Luminescent Materials and Devices, South China University of Technology, Guangzhou 510640, P. R. China. E-mail: mssjsu@scut.edu.cn*

† These authors contributed equally to this work.

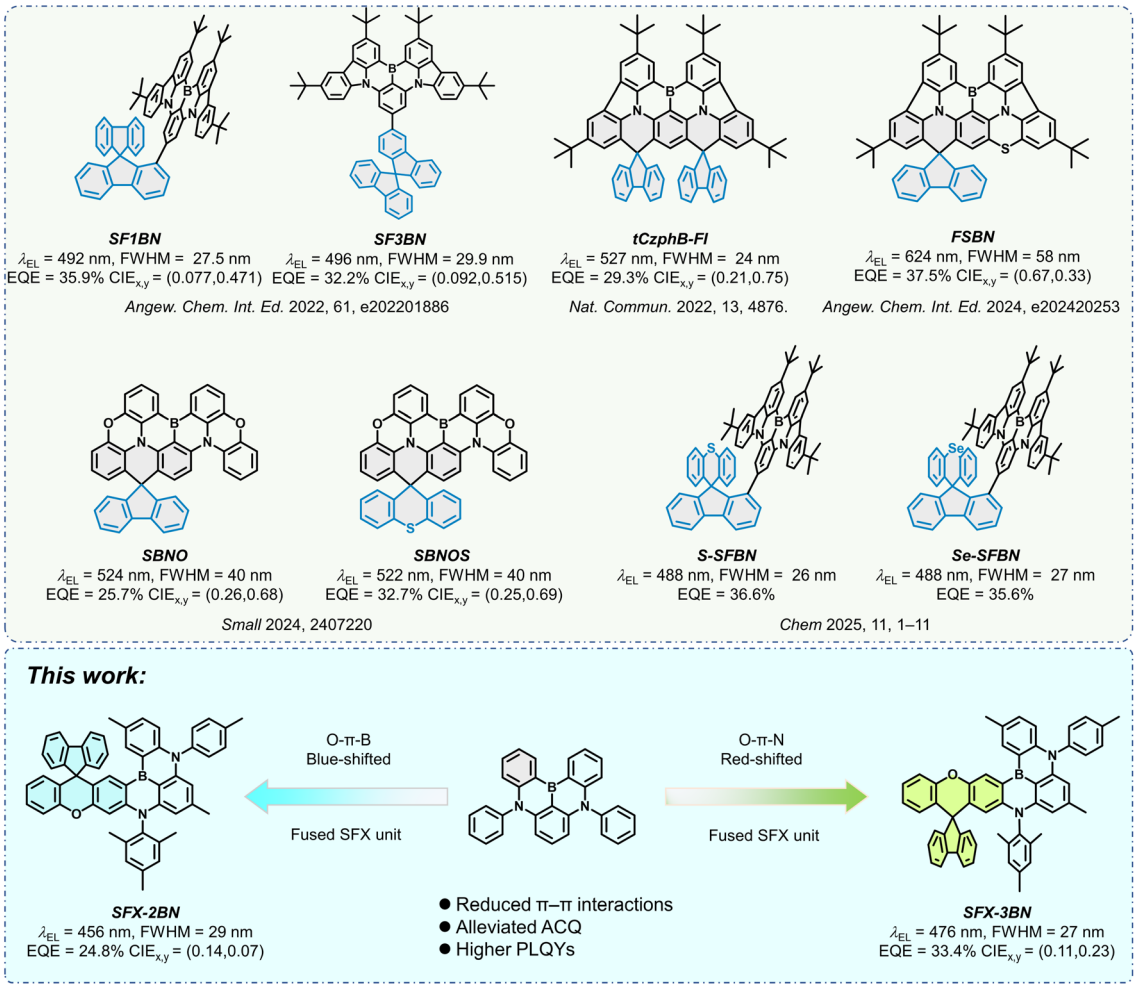

Fig. 1 MR-TADF emitters with spiro units and the molecular design strategy of SFX-2BN and SFX-3BN.

resulting in a red shift and a broadened emission spectrum (Fig. 1). Another technique is to modify the MR-TADF emitters with spiro units (Fig. 1). Jiang *et al.* incorporated the spiro unit (SBF) to develop sterically hindered MR-TADF emitters *via* simple mono-substitution, achieving improved performance and greater resistance to spectral broadening.[22] In 2024, an approach called "intramolecular external HAE" was utilized to dope heavy atoms into MR systems through the spiro frameworks, exhibiting nearly identical emission peaks to the parent emitter BNCz.[12] Furthermore, the spiral-locking strategy is also an effective way to resist ACQ and spectral broadening. Zhang *et al.* developed two green molecules by fixing the outer phenyl rings to the central phenyl ring in BNCz (DtBuCzB) using spiro-carbon formation, effectively suppressing the excited-state distortion and the vibration modes induced by the strong intramolecular charge transfer (ICT) effect.[23] Wang *et al.* introduced a novel and practical spiro-carbon locking and sulfur-embedding strategy to modify the BNCz MR-TADF framework, yielding a red emitter with high efficiency (50.1 lm W^{-1}) and a FWHM of 58 nm.[24] Li and Tang *et al.* incorporated a spiro-carbon bridge into the "bay area" of the MR-TADF compound (BNO), reducing intermolecular interactions between adjacent chromophores and thereby suppressing the ACQ effect and spectral broadening.[25] Li and Ge designed a molecular design strategy that incorporates the rigid 9,9′-spirobi[fluorene] (SF) unit, either fully or partially, into the B/N-MR emitting core,[26] achieving exceptionally narrow FWHM values (15–21 nm) in dilute toluene solutions and high photoluminescence quantum yields (PLQYs) up to 90% in doped films. Blue and sky-blue OLEDs with these emitters achieved the maximum efficiency of 29.8% and 35.5%, respectively. These strategies underscore the crucial role of spiro units in attaining high color purity for MR-TADF emitters. Most MR-TADF emitters with spiro structures mainly exhibit blue-green, green, and red emissions. However, reports on blue or deep-blue emitters are limited.

Herein, we present a molecular design strategy that peripherally fuses spiro[fluorene-9,9′-xanthene] (SFX) units at specific positions in the narrowband emitter DABNA core. This precise positional engineering yields two isomeric MR-TADF emitters, SFX-2BN (O-π-B) and SFX-3BN (O-π-N), showcasing exceptional potential for blue OLEDs. The spiro-rigidified skeleton acts as an intramolecular lock, effectively suppressing vibrational relaxation and π–π stacking, thereby achieving narrowband emission with minimal FWHM values (20–22 nm). Crucially, the

site-specific fusion strategy enables oxygen-atom-mediated spectral tuning: SFX-2BN exhibits a hypochromatic-shifted emission peak at 454 nm in toluene solution, while SFX-3BN displays a red-shifted peak at 475 nm. Peripheral spiro fusion suppresses intramolecular π-stacking and mitigates the aggregation-caused quenching (ACQ) effect, as evidenced by single-crystal X-ray analysis. Both emitters achieve high PLQYs over 90% in doped films and high-efficiency OLED performance. The SFX-2BN-based device achieves a maximum EQE of 24.8% with CIE coordinates of (0.14, 0.06) and a FWHM of 29 nm, while the EQE of the SFX-3BN-based device reaches 33.4% with CIE coordinates of (0.11, 0.20) and a FWHM of 27 nm. Notably, the SFX-2BN-based OLED achieves a CIEy of 0.06, closely approaching the BT.2020 blue standard. This work establishes spiro-fusion positional isomerism as an effective strategy for narrowing emission bands, thereby offering a novel paradigm for the development of high-efficiency blue narrowband emitters.

Results and discussion

The synthetic procedures of these two molecules are depicted in Scheme S1 (SI). The synthesis of these two target compounds is based on a one-pot boronation method,[14] giving high yields of the desired products. The preparation procedures and structural characterization details are described in the SI. The target compounds are purified through a sequential process involving column chromatography, recrystallization, and sublimation utilizing programmed gradient heating. Their structures were confirmed using ^{1}H NMR, ^{13}C NMR, high-resolution mass spectrometry, and single-crystal structure analysis. Thermal stability plays a critical role in the formation of stable films through chemical vapor deposition. The decomposition temperatures (T_d), defined as the temperatures corresponding to 5% weight loss, were determined to be 400.7 °C and 420.9 °C for SFX-2BN and SFX-3BN (Fig. S1), respectively. SFX-3BN exhibited a glass transition temperature (T_g) of 192.7 °C; however, no glass transition was detected for SFX-2BN. The excellent thermal stability of these molecules constitutes an essential prerequisite for the fabrication and application of OLEDs.

Single crystal structures can provide precise insights into the geometric configurations of new chemical compounds and their intermolecular interactions. Therefore, single-crystal cultivation was carried out at room temperature using a mixed solvent system of methanol and dichloromethane, and the resulting crystal structure was analyzed by X-ray diffraction. High-quality single crystals of SFX-3BN were successfully obtained; however, no suitable single crystals of SFX-2BN for structural analysis could be obtained despite repeated attempts. As illustrated in Fig. S2, the boron atom is incorporated into the anticipated reaction sites, forming hexagonal structures with the carbon and nitrogen atoms. As shown in Fig. S2, the dihedral angle between the SFX unit and the benzene unit is 19.89°. In addition, a large dihedral angle of 85.23° was observed between xanthene and fluorene in the SFX unit, resulting in the steric hindrance between the molecules, which can significantly reduce the π–π stacking interactions. Owing to the planar geometric characteristics, MR-TADF emitters are prone to experiencing significant solid-state quenching effects resulting from strong π–π stacking interactions. Interestingly, the crystal of SFX-3BN exhibits loose packing due to the introduction of the SFX unit. To elucidate the crystal packing behavior of SFX-3BN, a comprehensive analysis of the primary intermolecular interactions was performed through Hirshfeld surface analysis (Fig. 2 and S3).[27,28] The results indicate that the intramolecular stacking in SFX-3BN is predominantly governed by C–H···π interactions, with interatomic distances ranging from 2.723 to 2.863 Å and a contribution of 30.4%. Furthermore, C–H···B, C–H···O, and C–H···N interactions were also detected in the SFX-3BN crystal with contributions of 1.0%, 2.8% and 0.2%, respectively. As expected, the intramolecular π–π interactions between trimethylbenzene and fluorene within the SFX unit, with an interplanar distance of 4.745 Å, contribute only 0.6% in the single crystal, indicating that the incorporation of the spiro unit SFX significantly suppresses these interactions. These results further substantiate the critical role of the spiro structure in suppressing the aggregation of MR-TADF emitters.

To elucidate the underlying principles of our molecular design concepts, theoretical calculations were conducted using the Gaussian 16 software package, with particular emphasis on SFX-2BN and SFX-3BN. As depicted in Fig. 3, both materials possess classical MR characteristics with an alternating HOMO/LUMO mode. The HOMO distribution of SFX-2BN is predominantly localized on the B/N core, displaying an atomic-scale distribution pattern, with only a minor contribution from the xanthene moiety of the SFX units. In contrast, the HOMO of SFX-3BN extends across the entire xanthene moiety of the SFX unit, suggesting a relatively shallower HOMO level for SFX-3BN. Regarding the LUMO distribution, SFX-2BN shows a spread across the whole xanthene moiety of the SFX unit. The LUMO distribution of SFX-3BN is predominantly localized on the adjacent benzene ring of the xanthene moiety within the SFX unit. Since these two molecules are isomers, they exhibit similar electrostatic potential (ESP) distributions, as evidenced by the comparative analysis of the statistical data presented in Fig. S4. According to the calculated ESP maps (Fig. S5), the electron-deficient regions of the two molecules are predominantly distributed along the molecular units containing oxygen and boron atoms. In contrast, the electron-rich areas are primarily located on the nitrogen-connected units and the fluorene unit in SFX. Consequently, the calculated energy gap (E_g) of SFX-3BN is narrowed to 3.45 eV, and the singlet energy (S_1) is reduced to 2.89 eV. In contrast, the E_g and S_1 energy for SFX-2BN are 3.69 eV and 3.04 eV, respectively. This difference leads to the red-shifted emission observed in SFX-3BN compared to SFX-2BN. Furthermore, the excited-state properties of these compounds were further explored through time-dependent DFT (TD-DFT) to discuss the emission process. The natural transition orbitals (NTOs) of the S_1 and T_1 excited state have similar distributions to their HOMO and LUMO (Fig. S6). The $S_0 \rightarrow S_1$ and $S_0 \rightarrow T_1$ excitation of these two molecules are predominantly attributed to HOMO → LUMO transitions with contribution weights

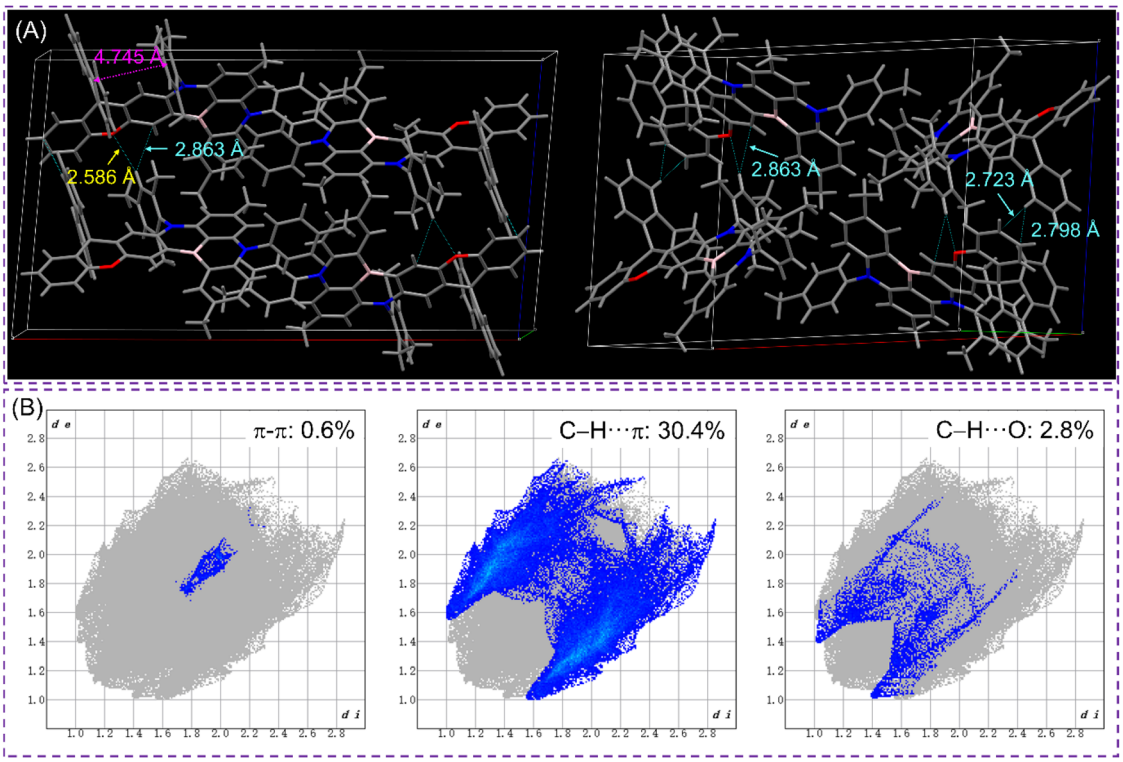

Fig. 2 (A) Packing patterns characterized by abundant C–H···π and C–H···O bonds and (B) the primary intermolecular interactions along with their respective proportions in the SFX-3BN crystal.

ranging from 96.1% to 98.7% (Table S3), demonstrating the predominantly SRCT-characterized S_1 and T_1 excited states of SFX-2BN and SFX-3BN.

Owing to the rigid structures of SFX-2BN and SFX-3BN, the geometrical deformation between the ground state (S_0) and S_1 state is observed with the root mean squared displacement

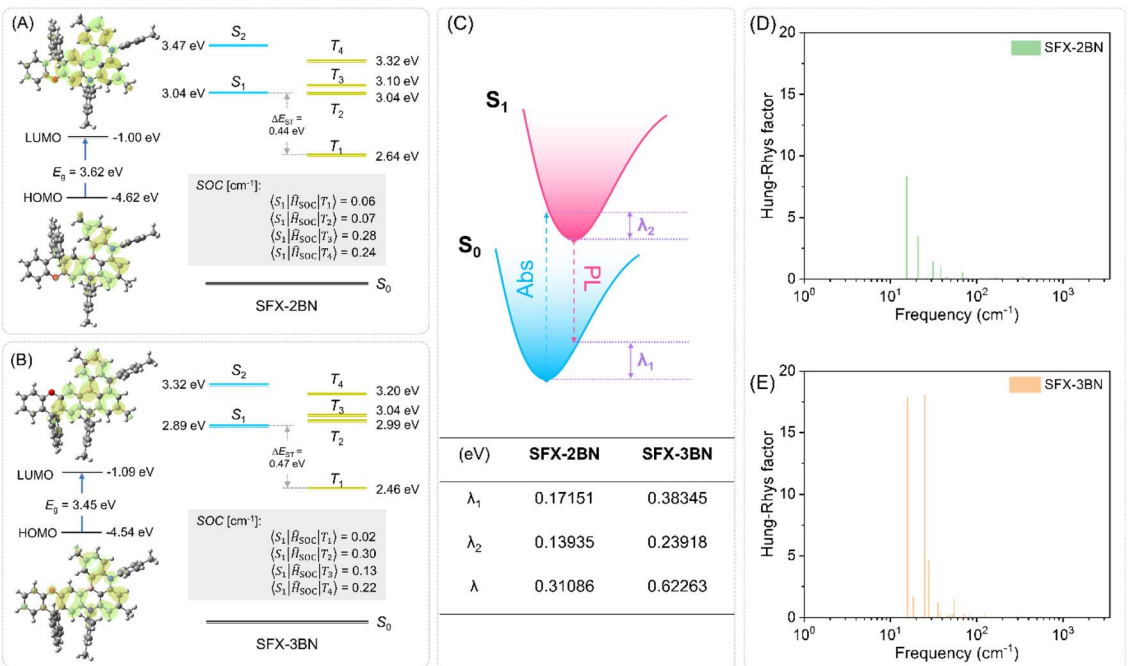

Fig. 3 The calculated FMO distribution, excited energy levels, SOC values (A and B), reorganization energy (λ) (C), and Huang–Rhys (HR) factor (D and E) for the $S_1 \rightarrow S_0$ transition of SFX-2BN and SFX-3BN, respectively.

(RMSD) of 0.334 and 0.540 Å, respectively (Fig. S7), demonstrating the suppression of excited state structural relaxation. To gain a better understanding of the mechanisms behind narrowband emission, we can quantify the reorganization energy (λ) and the coupling strength between structural changes and vibrational modes using the Huang–Rhys (HR) factor.[29,30] The calculated total λ values are 0.311 eV for SFX-2BN and 0.623 eV for SFX-3BN (Fig. 3, S8 and S9). These values indicate that molecular relaxation is suppressed, which facilitates narrowband emission. The relatively larger RMSD and λ value could be attributed to the significant molecular geometrical relaxation in S_1 states, as evidenced in Fig. S7 and S8. As illustrated in Fig. 3D and E, low-frequency vibrational modes (below 100 cm^{-1}) associated with bending, twisting, and rocking motions contribute significantly to the HR factors for the $S_1 \rightarrow S_0$ transition. These findings suggest that while high-frequency vibrations are effectively suppressed, the dominant low-frequency vibrational modes play a crucial role in achieving narrowband emission.[29,31]

Ultraviolet-visible (UV-vis) absorption and photoluminescence (PL) spectra of SFX-2BN and SFX-3BN were preliminarily characterized in dilute toluene solution (1×10^{-5} M). As displayed in Fig. 4, the intense and sharp absorption bands, which peak at 438 and 458 nm, respectively, are attributed to the short-range charge transfer (SRCT) character of SFX-2BN and SFX-3BN. The optical bandgaps (E_gs) are estimated to be 2.73 and 2.60 eV for SFX-2BN and SFX-3BN, respectively, from the onset of the absorption spectra. The PL spectra displayed strong and well-defined deep blue and pure blue emission, with emission peak wavelengths at 454 nm for SFX-2BN and 475 nm for SFX-3BN, respectively. Correspondingly, small FWHM values of 20 and 22 nm, as well as Stokes shifts of 16 and 17 nm, are obtained. This indicates a slight molecular geometrical relaxation between the ground and excited states, which can be attributed to its fully fused rigid molecular structure. Moreover, both emitters exhibit a weak solvation effect, with emission peaks shifting by less than 20 nm as the solvent changes from nonpolar *n*-hexane to polar dichloromethane (Fig. S10 and Table S5), a characteristic of MR-TADF emitters.[29,32,33] To evaluate the ΔE_{ST}s of SFX-2BN and SFX-3BN, the low-temperature fluorescence and phosphorescence spectra are recorded at 77 K in oxygen-free frozen toluene. As depicted in Fig. S11, the singlet energies (S_1) were determined to be 2.78 and 2.72 eV for SFX-2BN and SFX-3BN, respectively, while the triplet energies (T_1) were measured to be 2.67 and 2.54 eV. Accordingly, the ΔE_{ST} values were calculated to be 0.11 and 0.18 eV for SFX-2BN and SFX-3BN, respectively, indicating the potential RISC process and delayed fluorescence emission of these two molecules.

To investigate the TADF properties of SFX-2BN and SFX-3BN in the solid state, doped thin films were prepared using 9,9′-(1,3-phenylene)bis-9*H*-carbazole (mCP) as the host with a doping concentration of 3 wt%. As depicted in Fig. 4, deep-blue emission was observed for the SFX-2BN-doped film, with an emission peak at 456 nm and a FWHM of 26 nm. In contrast, the SFX-3BN-based film displayed blue emission with an emission peak at 476 nm and a FWHM of 28 nm. Both emitters demonstrated bathochromically shifted and broadened emission spectra in the solid state compared to their PL spectra in toluene, which can be attributed to the solid-state solvation effect, the π–π interaction between the host and dopant and the conformational change.[4,13,30,34] The transient PL decay curves of the doped films were measured and are presented in Fig. S12. Both emitters exhibited distinct secondary exponential decays, which indicate the TADF characteristics of these two emitters. For SFX-2BN and SFX-3BN doped films, clear prompt components with lifetimes (τ_{PF}) of 5.6 and 6.5 ns, as well as delayed components with lifetimes (τ_{DF}s) of 41.4 and 64.2 μs, were respectively recorded. The PLQYs of SFX-2BN and SFX-3BN (3 wt%) doped in the mCP host were measured to be 92.0% and 96.5% under a N_2 atmosphere, respectively, which could be attributed to the suppressed nonradiative decay originating from the rigid structure of these two emitters. Furthermore, the PLQYs of the prompt and delayed components are identified as 69.1% and 22.9% for SFX-2BN, and 78.6% and 17.9% for SFX-3BN, respectively. The radiative decay rates (k_r) for SFX-2BN and SFX-3BN were calculated to be 1.2×10^8 and 1.2×10^8 s^{-1} (Table S6), respectively. Additionally, the k_{RISC} values were estimated to be 2.6×10^4 and 1.7×10^4 s^{-1}, respectively. The relatively low k_{RISC} values can be attributed to the large ΔE_{ST} values of these two emitters.

Cyclic voltammetry was conducted to assess the energy levels of these two molecules (Fig. S13), with the results summarized in Table S4. The electrochemical HOMO levels were estimated based on the oxidative waves observed during the anodic sweep,

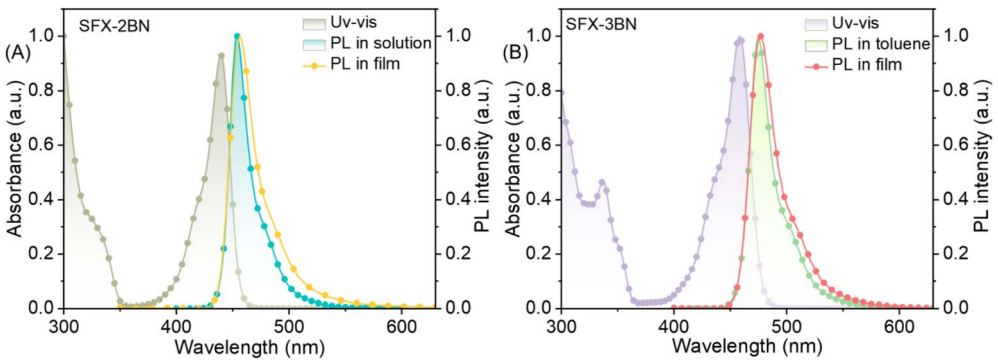

Fig. 4 The UV-vis absorption and PL spectra in dilute toluene (1×10^{-5} M) and mCP-doped films for SFX-2BN (A) and SFX-3BN (B).

yielding values of −5.37 and −5.44 eV for SFX-2BN and SFX-3BN, respectively. The LUMO energy levels were calculated to be −2.65 and −2.85 eV for SFX-2BN and SFX-3BN, respectively, from the HOMO energies and the optical bandgaps from the absorption onset.

To explore the potential of these two molecules as emitters for OLEDs, we systematically investigated their EL properties using devices with the following device architecture: ITO/HATCN (5 nm)/TAPC (30 nm)/TCTA (10 nm)/mCBP (10 nm)/EMLs (30 nm)/PPF (10 nm)/TmPyPB (40 nm)/LiF (0.5 nm)/Al (150 nm). In the EML, 7-((2′-methyl-[1,1′-biphenyl]-3-yl) oxy)-3,11-di-*o*-tolyl-5,9-dioxa-13b-boranaphtho[3,2,1-de]anthracene (DOBNA-OAr)[4] was selected as the host material. The doping concentrations were optimized to 1 wt% (Devices A and C for SFX-2BN and SFX-3BN, respectively) and 3 wt% (Devices B and D for SFX-2BN and SFX-3BN, respectively). ITO and Al are used as the anode and cathode, respectively. HAT-CN (1,4,5,8,9,11-hexaazatriphenylene hexacarbonitrile) and LiF were used as hole and electron-injection layers, respectively. TAPC (*N*-(4-(1-(4-(di-*p*-tolylamino)phenyl) cyclohexyl)phenyl)-3-methyl-*N*-(*p*-tolyl)aniline) and TCTA (4,4′,4″-tris(carbazol-9-yl)-triphenylamine) were employed as the hole-transporting layer (HTL), and TmPyPB (1,3,5-tri[(3-pyridyl)-phen-3-yl]benzene) served as the electron-transporting layer (ETL). mCBP (3,3′-di(9*H*-carbazol-9-yl)biphenyl) and PPF dibenzo[*b*,*d*]furan-2,8-diylbis(diphenylphosphine oxide) were utilized as the electron-blocking layer (EBL) and hole-blocking layer (HBL), respectively. The energy level diagram of the devices and molecular structures of the materials used are shown in Fig. 5A and S14. The EL spectra and device performance characteristics, including current densities (*J*), voltages (*V*), luminance (*L*), and efficiency, are presented in Fig. 5 and S15. The detailed device parameters are presented in Table 1.

As shown in Fig. 5B, except for Device A, all other devices exhibited EL spectra that closely resembled the corresponding PL spectra of their doped films, confirming that the EL emission originated exclusively from the emitters themselves *via* the same radiative decay process. Due to the low doping concentration, Device A, which employed SFX-2BN as the emitter at a doping concentration of 1 wt%, exhibited EL spectra featuring a minor contribution from the host material (DOBNA-OAr). Device A and Device B, both utilizing SFX-2BN as the emitter, exhibited deep-blue emission with peaks at 455 and 456 nm, and corresponding FWHMs of 29 nm each, respectively. In contrast, Devices C and D, based on SFX-3BN, displayed sky-blue emission with peaks at 476 and 477 nm and FWHMs of 27 and 27 nm, respectively. Owing to the strong host–dopant interactions resulting from the reduced intermolecular distances, both emitters exhibited a broader FWHM of emission in comparison to their PL spectra in the doped films.[35] Owing to the narrow EL spectra, Commission Internationale de l'Eclairage (CIE) coordinates of (0.14, 0.06) and (0.14, 0.07) for SFX-2BN, and (0.11, 0.20) and (0.11, 0.23) for SFX-3BN were obtained, respectively. Notably, the SFX-2BN-based OLEDs demonstrated exceptional color purity, as evidenced by a CIE_y value of 0.06, which closely aligns with the BT.2020 blue standard. The current–voltage–luminance (*J*–*V*–*L*) characteristics show that the devices have a turn-on voltage (V_{on}) of 2.9 to 3.1 V, indicating efficient carrier injection and transport properties. For SFX-2BN, a peak external quantum efficiency (EQE) of 24.8% and a current efficiency (CE) of 17.4 cd A^{-1} were achieved at a doping concentration of 3 wt%. This represents one of the most efficient devices reported to date, with $CIE_y \leq 0.1$ when utilizing a single-boron/nitrogen (B/N)-core structure (Fig. 5F and Table S7).[5,26,36–38] Due to the inefficient energy transfer from the host to the dopant at a doping concentration of 1 wt%, Device A exhibited a poor efficiency of 9.6%. In contrast, the SFX-3BN-based device achieved a maximum EQE of 33.4% at a doping concentration of 1 wt%, without the implementation

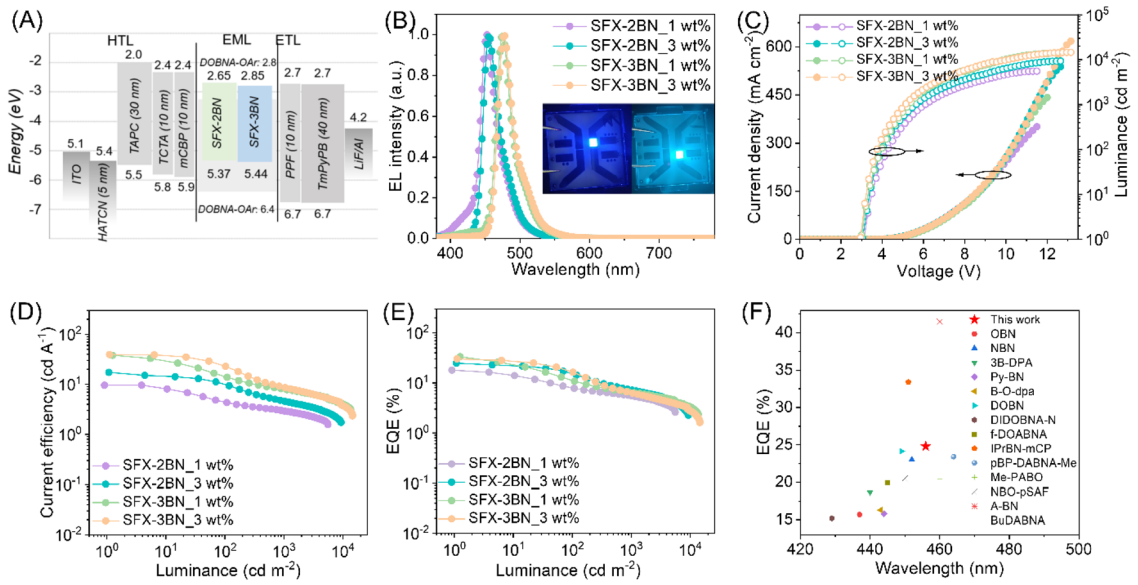

Fig. 5 (A) Schematic diagram of the device configuration, (B) the EL spectra, (C) *J*–*V*–*L* characteristics, (D and E) the efficiency curves of devices A–D, and (F) EQE *versus* wavelength of some representative blue OLEDs reported in the literature with $CIE_y \leq 0.1$.

Table 1 The EL properties of the OLEDs based on SFX-2BN and SFX-3BN

Device	V_{on}[a] [V]	L_{max}[b] [cd m^{-2}]	λ_{EL}[c] [nm]	FWHM[c] [nm]	CE[d] [cd A^{-1}]	PE[d] [lm W^{-1}]	EQE[d] [%]	CIE[e] [x, y]
A	3.1	5554	455	29	9.6	9.8	18.0	0.14, 0.06
B	3.0	9340	456	29	17.4	17.9	24.8	0.14, 0.07
C	3.0	13 683	476	27	38.2	40.0	33.4	0.11, 0.20
D	2.9	14 575	477	27	39.4	41.9	30.2	0.11, 0.23

[a] The turn-on voltages. [b] The maximum luminance. [c] The electroluminance spectral peaks and full width at half maximum detected at 6 V. [d] The maximum current efficiencies, the maximum power efficiencies, and the maximum external quantum efficiency. [e] The coordinates of CIE measured at 6 V.

of light outcoupling enhancement techniques (Fig. 5E and Table 1). When the doping concentration reached 3 wt%, the SFX-3BN-based device (D) showed inferior performance, with a maximum EQE of 30.2% and a maximum CE of 39.4 cd A^{-1}. However, all devices experienced significant efficiency roll-off. Specifically, the EQEs of Devices A–D were 5.0%, 8.5%, and 9.1%, respectively, at a luminance of 1000 cd m^{-2}. This pronounced efficiency roll-off is primarily attributed to severe triplet-related annihilation processes, which arise from their relatively long decay lifetimes.[39]

To effectively suppress the efficiency roll-off, a ternary system containing TADF sensitizer mMDBA-DI (5-(3,11-dimethyl-5,9-dioxa-13b-boranaphtho[3,2,1-de]anthracen-7-yl)-10,15-diphenyl-10,15-dihydro-5*H*-diindolo[3,2-a:3′,2′-c]carbazole)[40] and the PPF host in the EML was adopted to assist the up-conversion process of triplet excitons under electrical excitation. As shown in Fig. S16, spectral overlap between the UV-vis absorption spectra of emitters and the PL spectra of the TADF sensitizer can be observed, indicating efficient Förster resonance energy transfer (FRET) from mMDBA-DI to SFX-2BN and SFX-3BN (Fig. S16). Based on the above findings, the optimized OLEDs were further fabricated using the aforementioned device structure with PPF, mMDBA-DI, and SFX-2BN/SFX-3BN as the EML, with the proportions of each component set at 67%, 30%, and 3%, respectively. As demonstrated in Fig. S17 and Table S8, bathochromic-shifted emission peaking at 464 and 483 nm, accompanied by significant improvement of FWHM to 41 and 38 nm for SFX-2BN and SFX-3BN, respectively, in comparison with that of the device utilizing the conventional DOBNA-OAr host, was observed for the sensitized device, with corresponding CIE coordinate of (0.14, 0.15) and (0.11, 0.32). The V_{on}s of both devices were similar to those of the non-sensitized devices, with V_{on}s of 3.0 and 3.1 V. Furthermore, these two devices achieved a maximum luminance of over 10 000 cd m^{-2} and desirable maximum EQEs of over 27%, along with reduced efficiency roll-offs. For example, a maximum EQE of 27.5% and a CE of 32.8 cd A^{-1} were obtained for the SFX-2BN-based device, and the EQE remained relatively high at a luminance of 100 cd m^{-2} (22.3%), indicating efficient suppression of triplet-related quenching by the sensitizer.[41]

Conclusions

In conclusion, we propose a novel molecular design strategy for MR-TADF emitters *via* site-specific peripheral fusion of rigid spiro architectures. This strategy enforces molecular rigidity to suppress vibrational relaxation and intramolecular π–π stacking, enabling two regioisomeric emitters, SFX-2BN (O-π-B) and SFX-3BN (O-π-N), to serve as high-performance blue OLED candidates. Crucially, the regioisomerism-controlled positioning of boron, nitrogen, and oxygen atoms within the spiro unit allows for precise emission tuning. SFX-2BN achieves an exceptional pure-blue emission of 454 nm, with an FWHM of 20 nm in a toluene solution. In comparison, SFX-3BN exhibits sky-blue characteristics of 476 nm, with an FWHM of 22 nm under the same conditions. Both emitters demonstrate PLQYs greater than 90% in doped films. Their OLEDs achieve maximum EQEs of 24.8% (SFX-2BN) and 33.4% (SFX-3BN). Notably, by incorporating an efficient TADF assistant host, the maximum EQE of the SFX-2BN-based device is further improved to 27.5%. Moreover, the SFX-2BN-based OLED achieves exceptional color purity with CIE coordinates of (0.14, 0.06), which closely approach the stringent BT.2020 blue standard. This study demonstrates that the spiro-fusion positional strategy not only effectively narrows emission bands but also enhances electroluminescent efficiencies, offering a novel design principle for the development of high-performance blue narrowband emitters.

Author contributions

Deli Li, Denghui Liu and Mengke Li contributed equally to this work. Deli Li: conceptualization, investigation, formal analysis, funding acquisition, visualization, writing – original draft, methodology. Denghui Liu: investigation, formal analysis. Mengke Li: formal analysis, investigation, resources. Qingchao Liu: investigation. Wei Liu: investigation, conceptualization. Wei Li: writing – review & editing, supervision. Shi-Jian Su: writing – review & editing, supervision. Xuchuan Jiang: writing – review & editing, project administration.

Conflicts of interest

There are no conflicts to declare.

Data availability

CCDC 2408451 contains the supplementary crystallographic data for this paper.[42]

The data (experimental methods, synthetic procedures, structural characterization data including NMR and MS spectra, theoretical calculations, thermodynamics data, crystallographic data, and device performance data) that support this article are available in the article itself and its SI. Supplementary information is available. See DOI: **https://doi.org/10.1039/d5sc05501f**.

Acknowledgements

The authors greatly appreciate the financial support from the National Natural Science Foundation of China (22305086, 22522512) and the Natural Science Foundation of Shandong Province (ZR2024QB123).

Notes and references

1 T. Hatakeyama, K. Shiren, K. Nakajima, S. Nomura, S. Nakatsuka, K. Kinoshita, J. Ni, Y. Ono and T. Ikuta, *Adv. Mater.*, 2016, **28**, 2777–2781.
2 N. Ikeda, S. Oda, R. Matsumoto, M. Yoshioka, D. Fukushima, K. Yoshiura, N. Yasuda and T. Hatakeyama, *Adv. Mater.*, 2020, **32**, e2004072.
3 J. Miao, G. Chen, J. He, Z. Xiao, X. Song, M. Wang, M. Huang, K. Li, X. Cao, Y. Zou and C. Yang, *Adv. Funct. Mater.*, 2024, **34**, 2316323.
4 Y. Kondo, K. Yoshiura, S. Kitera, H. Nishi, S. Oda, H. Gotoh, Y. Sasada, M. Yanai and T. Hatakeyama, *Nat. Photon.*, 2019, **13**, 678–682.
5 X. Cai, Y. Pan, C. Li, L. Li, Y. Pu, Y. Wu and Y. Wang, *Angew. Chem., Int. Ed.*, 2024, **63**, e202408522.
6 E. Ravindran, H. E. Baek, H. W. Son, J. H. Park, Y. H. Kim and M. C. Suh, *Adv. Funct. Mater.*, 2023, **33**, 2213461.
7 Y. Yuan, X. Tang, X. Y. Du, Y. Hu, Y. J. Yu, Z. Q. Jiang, L. S. Liao and S. T. Lee, *Adv. Optical Mater.*, 2019, **7**, 1801536.
8 F. Huang, K. Wang, Y. Z. Shi, X. C. Fan, X. Zhang, J. Yu, C. S. Lee and X. H. Zhang, *ACS Appl. Mater. Interfaces*, 2021, **13**, 36089–36097.
9 T. Feng, X. Nie, D. Liu, L. Wu, C. Y. Liu, X. Mu, Z. Xin, B. Liu, H. Qi, J. Zhang, W. Li, S. J. Su and Z. Ge, *Angew. Chem., Int. Ed.*, 2025, **64**, e202415113.
10 M. Li, R. Li, Z. Li, Z. Chen, D. Liu, Z. Yang, H. Xie, K. Liu and S. J. Su, *Adv. Optical Mater.*, 2024, **13**, 2402822.
11 R.-Z. An, F.-M. Zhao, C. Shang, M. Zhou and L. Cui, *Angew. Chem., Int. Ed.*, 2025, **64**, e202420489.
12 Q. Zheng, Y.-K. Qu, P. Zuo, H.-T. Yuan, Y.-J. Yang, Y.-C. Qiu, L.-S. Liao, D.-Y. Zhou and Z.-Q. Jiang, *Chem*, 2025, **11**, 1–11.
13 P. Jiang, J. Miao, X. Cao, H. Xia, K. Pan, T. Hua, X. Lv, Z. Huang, Y. Zou and C. Yang, *Adv. Mater.*, 2022, **34**, e2106954.
14 Y. Zhang, J. Wei, D. Zhang, C. Yin, G. Li, Z. Liu, X. Jia, J. Qiao and L. Duan, *Angew. Chem., Int. Ed.*, 2022, **61**, e202113206.
15 J. Bian, S. Chen, L. Qiu, R. Tian, Y. Man, Y. Wang, S. Chen, J. Zhang, C. Duan, C. Han and H. Xu, *Adv. Mater.*, 2022, **34**, e2110547.
16 D. Li, M. Li, W. Li, W. Li, Z. Chen, X. Peng, D. Liu, G.-X. Yang, S. Jiang, Y. Gan, Z. Yang, K. Liu and S.-J. Su, *Chem. Eng. J.*, 2023, **458**, 141416.
17 W. Li, M. Li, W. Li, Z. Xu, L. Gan, K. Liu, N. Zheng, C. Ning, D. Chen, Y. C. Wu and S. J. Su, *ACS Appl. Mater. Interfaces*, 2021, **13**, 5302–5311.
18 M. Liu, R. Komatsu, X. Y. Cai, K. Hotta, S. Sato, K. K. Liu, D. C. Chen, Y. Kato, H. Sasabe, S. Ohisa, Y. Suzuri, D. Yokoyama, S. J. Su and J. Kido, *Chem. Mater.*, 2017, **29**, 8630–8636.
19 Z. Q. Jiang, R. H. Liu, Z. Q. Feng, S. J. Ge, Y. Wang, Z. H. Yu, J. R. Wu, H. Y. Yan, D. Y. Zhou and L. S. Liao, *Angew. Chem., Int. Ed.*, 2025, **64**, e202424950.
20 Y. J. Yang, D. Ari, Z. H. Yu, K. Lettelier, O. Jeannin, Q. Zheng, A. Khan, C. Quinton, D. Y. Zhou, J. Zuo-Quan and C. Poriel, *Angew. Chem., Int. Ed.*, 2025, **64**, e202501895.
21 W. Li, B. Li, X. Cai, L. Gan, Z. Xu, W. Li, K. Liu, D. Chen and S. J. Su, *Angew. Chem., Int. Ed.*, 2019, **58**, 11301–11305.
22 Y. K. Qu, D. Y. Zhou, F. C. Kong, Q. Zheng, X. Tang, Y. H. Zhu, C. C. Huang, Z. Q. Feng, J. Fan, C. Adachi, L. S. Liao and Z. Q. Jiang, *Angew. Chem., Int. Ed.*, 2022, **61**, e202201886.
23 J. Liu, Y. Zhu, T. Tsuboi, C. Deng, W. Lou, D. Wang, T. Liu and Q. Zhang, *Nat. Commun.*, 2022, **13**, 4876.
24 Y. Pu, X. Cai, Y. Qu, W. Cui, L. Li, C. Li, Y. Zhang and Y. Wang, *Angew. Chem., Int. Ed.*, 2025, **64**, e202420253.
25 H. Z. Li, F. M. Xie, J. Y. Bai, K. Zhang, H. N. Shi, J. Y. Liu, X. Li, J. X. Tang and Y. Q. Li, *Small*, 2024, **20**, e2407220.
26 L. Wu, C. Liu, D. Liu, D. Li, W. Li, J. Zhang, X. Mu, Z. Xin, B. Liu, H. Qi, Z. Wang, D. Liu, S. J. Su, Y. Zhou, S. Wu and Z. Ge, *Angew. Chem., Int. Ed.*, 2025, **64**, e202504723.
27 C. E. Galvez, O. E. Piro, G. A. Echeverría, K. Vignesh, S. Thamotharan, M. d. H. Loandos and D. M. Gil, *CrystEngComm*, 2025, **27**, 3806–3822.
28 P. R. Spackman, M. J. Turner, J. J. McKinnon, S. K. Wolff, D. J. Grimwood, D. Jayatilaka and M. A. Spackman, *J. Appl. Crystallogr.*, 2021, **54**, 1006–1011.
29 S. Jiang, Y. Yu, D. Li, Z. Chen, Y. He, M. Li, G. X. Yang, W. Qiu, Z. Yang, Y. Gan, J. Lin, Y. Ma and S. J. Su, *Angew. Chem., Int. Ed.*, 2023, **62**, e202218892.
30 D. L. Li, M. K. Li, D. H. Liu, J. J. Yang, W. Li, Z. H. Yang, H. X. Yuan, S. M. Jiang, X. M. Peng, G. X. Yang, W. T. Xie, W. D. Qiu, Y. Y. Gan, K. K. Liu and S. J. Su, *Adv. Optical Mater.*, 2023, **11**, 2301084.
31 X. Qiu, G. Tian, C. Lin, Y. Pan, X. Ye, B. Wang, D. Ma, D. Hu, Y. Luo and Y. Ma, *Adv. Optical Mater.*, 2020, **9**, 2001845.
32 K. Zhang, X. Wang, M. Wang, S. Wang and L. Wang, *Angew. Chem., Int. Ed.*, 2025, **64**, e202423812.
33 X. Wang, T. Hua, N. Li, G. Chen, Z. Chen, J. Miao, X. Cao and C. Yang, *Chem. Sci.*, 2025, **16**, 7495–7502.
34 D. Y. Chen, H. Wang, F. Huang, D. B. Cordes, A. P. McKay, K. Wang, X. H. Zhang and E. Zysman-Colman, *Adv. Funct. Mater.*, 2025, 2506189.
35 J. Han, Z. Huang, X. Lv, J. Miao, Y. Qiu, X. Cao and C. Yang, *Adv. Optical Mater.*, 2021, **10**, 2102092.
36 J. Jin, C. Duan, H. Jiang, P. Tao, H. Xu and W. Y. Wong, *Angew. Chem., Int. Ed.*, 2023, **62**, e202218947.

37 S. M. Suresh, L. Zhang, T. Matulaitis, D. Hall, C. Si, G. Ricci, A. M. Z. Slawin, S. Warriner, D. Beljonne, Y. Olivier, I. D. W. Samuel and E. Zysman-Colman, *Adv. Mater.*, 2023, **35**, e2300997.

38 S. Madayanad Suresh, L. Zhang, D. Hall, C. Si, G. Ricci, T. Matulaitis, A. M. Z. Slawin, S. Warriner, Y. Olivier, I. D. W. Samuel and E. Zysman-Colman, *Angew. Chem., Int. Ed.*, 2023, **62**, e202215522.

39 L. Chen, Y. Chang, H. Shu, Q. Li, S. Shi, S. Wang and L. Wang, *Adv. Optical Mater.*, 2022, **11**, 2201898.

40 K. R. Naveen, H. Lee, R. Braveenth, D. Karthik, K. J. Yang, S. J. Hwang and J. H. Kwon, *Adv. Funct. Mater.*, 2021, **32**, 2110356.

41 C. Yin, D. Zhang, Y. Zhang, Y. Lu, R. Wang, G. Li and L. Duan, *CCS Chem.*, 2020, **2**, 1268–1277.

42 D. Li, D. Liu, M. Li, Q. Liu, W. Liu, W. Li, S.-J. Su, X. Jiang, CCDC 2408451, Experimental Crystal Structure Determination, 2025, DOI: **10.5517/ccdc.csd.cc2lv5zm**.